

Cohesive sediment transport in the 3D-hydrodynamic-baroclinic circulation model, study case for idealized tidal inlet

Wahyu W. Pandoe*, Billy L. Edge

Ocean Engineering Program, Department of Civil Engineering, Texas A&M University, College Station, Texas 77843-3136, USA

Received 7 November 2003; accepted 22 April 2004

Abstract

This work provides a general hydrodynamic circulation model that can be used to understand density driven flows, which may arise in the case of suspension of fine-grained materials. The research is expected to provide a better understanding of the characteristics of spatial and temporal variability of current, which is associated with the period of ebb and flood tidal cycles.

The model development includes extending the existing three-dimensional (3D) ADCIRC model with (1) baroclinic forcing term and (2) transport module of suspended and soluble materials. The transport module covers the erosion, material suspension and deposition processes for cohesive type sediment. In the case of an idealized tidal inlet in stratified water, the inclusion of baroclinic term can demonstrate the prevailing longshore sediment transport. It is shown that the model has application to the transport of the cohesive sediments from the mouth of the Mississippi River along the north shore of the Gulf of Mexico towards and along the Texas coast.

© 2004 Elsevier Ltd. All rights reserved.

Keywords: Three-dimensional; Baroclinic; Saline wedge; Cohesive sediment transport; Longshore transport

* Corresponding author. Tel.: +1-979-845-0273; fax: +1-979-862-8162.
E-mail address: wpandoe@tamu.edu (W.W. Pandoe).

1. Introduction

Shoaling processes in a bay is presumed to correlate with the flow pattern in the estuary driven by tide generating current and wind stress. Sediment conveyed by river runoff to the estuary might also be one of the sedimentation sources.

The equation of motion shows that water moves in response to differences in pressure, which are generated by two factors: water surface slope (barotropic) and horizontal water density differences (baroclinic). The determination of barotropic and baroclinic flow is important since it may cause a convergence zone, where the converging pressure gradients drive internal circulation patterns into a common point. The baroclinic term may also cause dissimilarities between ebb and flood tidal currents. The presence of baroclinic-forced currents may strengthen the existence of the reverse estuarine flow.

The scope of this study is to implement and expand the hydrodynamic numerical modeling system to accommodate these density driven flows for an estuarine zone. The model used here is the three-dimensional (3D) version of Advanced Circulation (ADCIRC) Hydrodynamic Model (Luettich and Westerink, 2003) with extended transport module. ADCIRC is a finite element model used for hydrodynamic circulation problems. The model is based on the finite element codes that solve the shallow water equation on unstructured grids. Fine grid resolution can be specified locally to meet the accuracy requirements, and coarse resolution can be implemented in area distant from the region of interest. In the 3D-ADCIRC model, the baroclinic term might be appropriate to explain the variability of vertical current shear, which may alter sediment concentration vertically.

In the case of density stratification as a result of either little tidal action or with large freshwater (river) flow, the flow profile can be separated into two portions in the seaward regions of the tidal intrusion: (a) the upper part is the freshwater flow with little mixing to the seaward, and (b) the lower part is the saline water originating from the ocean water, that is called the ‘salinity wedge’ (Ippen, 1966; Partheniades, 1990). With the inclusion of the baroclinic term in the model development for the idealized estuarine model, the existence of a salinity wedge is distinctive penetrating to the river upstream. The objective of this research is to identify the circulation patterns of the water and sediment fluxes in an estuarine zone. Suspended materials in the water column are highly related to the hydrodynamic circulation. The interface of the salinity wedge or a convergence zone may be related to the presence of accumulation of deposited sediments.

2. Model description

2.1. Hydrodynamic

In this 3D circulation model, the vertical finite element domain will be divided into a number of sigma (σ) layers ranging from -1 at the bottom to 1 at the surface. In some cases, high gradients may occur at the bottom and surface, thus nor-

mally the vertical grids have higher density around the bottom and surface and lower density in the mid layers.

Water surface elevation is solved in a vertically integrated continuity equation utilizing the generalized wave continuity equation (GWCE) formulation. The modified GWCE is derived as a summation of the time derivative of the continuity equation and the spatial gradient of the momentum equations. The GWCE is used to solve the sea level elevations. The complete formulation of GWCE is given in Luetlich et al. (1992). The primitive form of the conservation of mass is:

$$\frac{\partial H}{\partial t} + \frac{\partial(UH)}{\partial x} + \frac{\partial(VH)}{\partial y} = 0 \quad (1)$$

where U and V are depth-averaged velocities, $H = h + \eta$, h is a bathymetric depth and η is a free surface elevation relative to the geoid.

The 3D version of ADCIRC applies the non-conservative form of the momentum equations to solve horizontal velocity u and v . The free surface elevation as described in Eq. 1 is solved by substituting the vertically integrated momentum equations into the continuity equation to form the GWCE. The momentum equations applied in ADCIRC-3D (Luetlich and Westerink, 2003) are:

$$\begin{aligned} \frac{\partial u}{\partial t} + u \frac{\partial u}{\partial x} + v \frac{\partial u}{\partial y} + \omega \left(\frac{a-b}{H} \right) \frac{\partial u}{\partial \sigma} - fv \\ = -g \frac{\partial \eta}{\partial x} + m_{x_\sigma} - b_{x_\sigma} + \left(\frac{a-b}{H} \right) \frac{\partial}{\partial \sigma} \left(\frac{\tau_{zx}}{\rho_0} \right) \end{aligned} \quad (2)$$

$$\begin{aligned} \frac{\partial v}{\partial t} + u \frac{\partial v}{\partial x} + v \frac{\partial v}{\partial y} + \omega \left(\frac{a-b}{H} \right) \frac{\partial v}{\partial \sigma} + fu \\ = -g \frac{\partial \eta}{\partial y} + m_{y_\sigma} - b_{y_\sigma} + \left(\frac{a-b}{H} \right) \frac{\partial}{\partial \sigma} \left(\frac{\tau_{zy}}{\rho_0} \right) \end{aligned} \quad (3)$$

where u and v are velocities in the x - and y -direction; ω , vertical velocity in σ -coordinate; f , Coriolis force; g , gravity acceleration; m_{x_σ} , combined horizontal diffusion/dispersion momentum; b_{x_σ} and b_{y_σ} , baroclinic pressure term in x - and y -directions; τ_{zx} and τ_{zy} , component of vertical shear stress; and ρ_0 , reference density of water.

Velocities are determined from the non-conservative form of the momentum equation. The solution strategy for solving horizontal velocities u and v in Eqs. (2) and (3) includes finite element method for spatial and finite difference for temporal. The vertical grid nodes are defined vertically at each horizontal node, thus the horizontal and vertical integrations can be performed independently. The detail of the 3D-VS formulations is given in Luetlich and Westerink (2003).

Vertical velocity is solved by the first derivative approach with the adjoint correction. Pandoe and Edge (2003) solved for ω in σ -coordinate, with essential boundary condition $\omega = 0$ at $\sigma = b$, and natural boundary condition $\delta\omega = 0$ at

$\sigma = a$:

$$\omega_{k+1} - \omega_k = -\frac{1}{(a-b)} \int_k^{k+1} \left(\frac{\partial \eta}{\partial t} + \frac{\partial(uH)}{\partial x} + \frac{\partial(vH)}{\partial y} \right) \partial \sigma \quad (4)$$

where k is a node number of a vertical element. The solution ω_k will satisfy the bottom boundary condition only. In order to satisfy the free surface, the adjoint correction is applied to Eq. (4) based on Luetlich and Muccino (2001) and Muccino et al. (1997).

2.2. Salinity/temperature/tracer transport model

The general governing equation for transport of salinity, temperature and tracer concentration (Blumberg and Mellor, 1987; Scheffner, 1999; Helfand et al., 1999; and HydroQual, 1998) is summarized as follows:

$$\begin{aligned} \frac{\partial R}{\partial t} + u \frac{\partial R}{\partial x} + v \frac{\partial R}{\partial y} + \frac{(a-b)}{H} (\omega - \omega_s) \frac{\partial R}{\partial \sigma} \\ = \frac{\partial}{\partial x} \left(D_h \frac{\partial R}{\partial x} \right) + \frac{\partial}{\partial y} \left(D_h \frac{\partial R}{\partial y} \right) + \left(\frac{a-b}{H} \right)^2 \frac{\partial}{\partial \sigma} \left[D_v \frac{\partial R}{\partial \sigma} \right] \end{aligned} \quad (5)$$

where R is either salinity [psu], heat [calories] or a tracer concentration [g/l or kg/m³]; D_h and D_v are horizontal and vertical dispersion coefficients [m²/s]; ω is vertical velocities in σ -coordinate [m/s]; and ω_s is settling velocity of sediment in σ -coordinate [m/s].

The surface and bottom boundary conditions of Eq. (5) for vertical salinity gradient are zero, while the surface boundary condition for temperature is given as

$$\left(\frac{a-b}{H} \right) \left(D_v \frac{\partial R}{\partial \sigma} \right) = \frac{Q_{shf}}{\rho_0 C_p} \quad \text{at } z \rightarrow \eta \quad (6)$$

The temperature transport formulation differs slightly from that for salinity. In the temperature formulation, the external effect of solar radiation, called surface net heat flux (Q_{shf}) is included. It has been shown that the mean value of net heat flux at the surface is 165 W/m² with standard deviation of 10 W/m² (Hayes et al., 1991). C_p is the specific heat of sea water [J/kg/°C] given as $C_p \approx 3.94 \times 10^3$ J/kg/°C.

In the development of the ADCIRC transport, the horizontal diffusion coefficient, D_h , is assumed constant within the range of 0.1–10 m²/s (Gross et al., 1999). The level 2.5 Turbulence Closure Model of Mellor and Yamada (1982) is used to calculate the vertical eddy diffusivity D_v .

2.3. Baroclinic forcing terms

Robertson et al. (2001) applied normalized density in order to reduce the truncation error in the computation of the baroclinic pressure gradient in the Princeton Ocean Model (POM). Thus, the normalized baroclinic forcing terms in Eqs. (2)

and (3) on ADCIRC-3D can be represented as

$$b_x = \frac{g}{\rho_0} \int_z^\eta \frac{\partial}{\partial x} (\rho - \rho_0) dz = \text{baroclinic } x - \text{forcing} \quad (7a)$$

$$b_y = \frac{g}{\rho_0} \int_z^\eta \frac{\partial}{\partial y} (\rho - \rho_0) dz = \text{baroclinic } y - \text{forcing} \quad (7b)$$

where η is a free surface elevation, and ρ_0 is a general mean density, which was set to 1000 (or 1025) kg/m³. The baroclinic terms $b_{x\sigma}$ and $b_{y\sigma}$ are a function of density distribution. The variable density is determined from temperature T , salinity S and pressure p using the *International Equation of State of Sea Water, IES80*.

The barotropic term is constant with depth, in contrast to the baroclinic term, which varies with depth (Fig. 1). The interaction of these two terms can create tidal asymmetry between the ebb and the flood of tidal cycle. During the flood current, the baroclinic and barotropic term could be additive producing high acceleration near the bed, and vice versa during ebb current. In the regions where the density gradient of the sea is most pronounced such as in estuarine and coastal regions, the condition of baroclinicity is the most extreme. Generally, the baroclinic situation can be found in the surface layer with the barotropic conditions being approached at greater depth.

2.4. Suspended sediment transport model

The general governing equation for sediment concentration (HydroQual, 1998) is similar to Eq. (5), but with boundary conditions:

$$\left(\frac{a-b}{H} \right) D_h \frac{\partial C}{\partial \sigma} = -\omega_s C_k \quad \text{at } z \rightarrow \eta \quad (8a)$$

$$\left(\frac{a-b}{H} \right) D_h \frac{\partial C}{\partial \sigma} = E - D \quad \text{at } z \rightarrow -h \quad (8b)$$

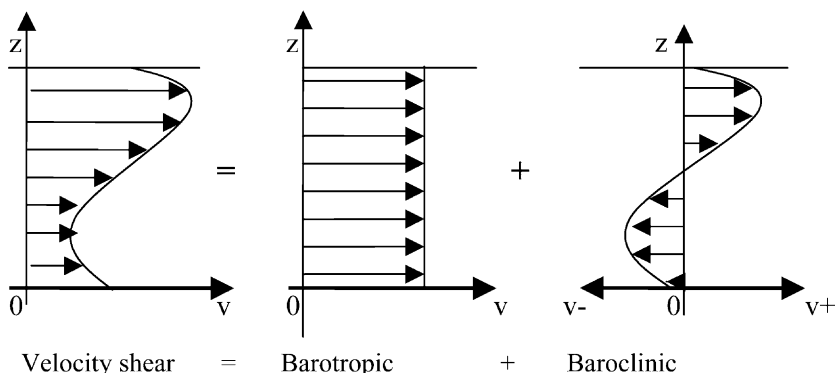


Fig. 1. The influence of barotropic and baroclinic terms on the vertical velocity shear.

where C is a sediment concentration [g/l or kg/m³]; E is an erosion flux [kg/m²/s]; and D is a deposition flux [kg/m²/s].

For cohesive type of sediment, Whitehouse et al. (2000) assumed that the flocs of cohesive sediment could be treated as low-density grains, when aggregation of flocs, break-up of flocs and water flow within flocs are neglected. The corresponding formula of settling velocity w_s is given as

$$w_s = \frac{v}{d_e} \left\{ [10.36^2 + 1.049(1 - C_f)^{4.7} D_*^3]^{1/2} - 10.36 \right\} \quad (9)$$

where $D_* = d_e[g(\rho_e - \rho)/\rho v^2]^{1/3}$ is a dimensionless floc diameter; d_e is the effective diameter of a floc that increases with the volume concentration C of the suspension; ρ is water density; ρ_e is effective density of the floc; C_f is the volume concentration of flocs in water [non-dimension]; and C_k is the mass concentration of the suspension [mass/volume].

The depositional flux rate is computed using the following settling formulation for cohesive sediment:

$$D = P w_s C_b$$

where

$$P = \text{probability of deposition} = \begin{cases} -(1 - \tau_b/\tau_{cd}) & \text{for } \tau_b < \tau_{cd} \\ 0 & \text{for } \tau_b \geq \tau_{cd} \end{cases} \quad (10)$$

with w_s , sediment settling velocity (m/s); and τ_{cd} is a critical bed shear stress and is estimated from laboratory tests to be between 0.06 and 0.10 N/m².

The analysis to estimate the erosion flux rate (E) expressed as dry mass of mud eroded per unit area per unit time (kg m⁻² s⁻¹) as a function of shear stress is given by Partheniades (1990) and Whitehouse et al. (2000):

$$\begin{aligned} E &= m_e(\tau_b - \tau_{ce}), & \tau_b > \tau_{ce} \\ E &= 0, & \tau_b \leq \tau_{ce} \end{aligned} \quad (11)$$

where m_e is an experimental/site specific erosion constant with $m_e = 0.0002 - 0.002 \text{ kN}^{-1} \text{ s}^{-1}$ and τ_{ce} is the critical bed shear stress for erosion given in Whitehouse et al. (2000) as

$$\tau_{ce} = 0.015(\rho_b - 1000)^{0.73} \quad (12)$$

Typical τ_{ce} is around 0.1–0.2 N/m² but it should not exceed 1.0 N/m², where ρ_b is the bulk density of the bed over the density range 1000–2000 kg/m³.

3. Model validation

The results of hydrodynamic velocity components u , v and w are compared to some analytical solutions to provide validation since experimental and field data are not available. Three-dimensional analytical solution of Lynch and Officer (1985) is applied here, which is also available in Muccino et al. (1997). Pandoe and

Edge (2003) have shown a good agreement for the hydrodynamic solution between the model and analytical solutions for the Quarter Annular Test Problem (QATP).

The benchmarking of the stratification due to the presence of the baroclinic terms will be performed using the theoretical ‘saline wedge’ formulation provided by Partheniades (1990). The comparison against theoretical length of saline wedge will be discussed by implementing the idealized riverine–ocean domain shown in Fig. 2. The ocean and river grid dimensions are 40 km alongshore, 24 km from the shoreline to the ocean boundary, and river length and width of 10 and 1 km, respectively. The river has uniform depth of 4 m, and the ocean has a sloped bottom from 4 m depth at the shoreline down to 23 m depth along the open ocean boundary.

In this case, the model is driven by the 0.1 m amplitude of M2 tide in the open ocean boundary (left side), and by the influx of normal riverine flow with a

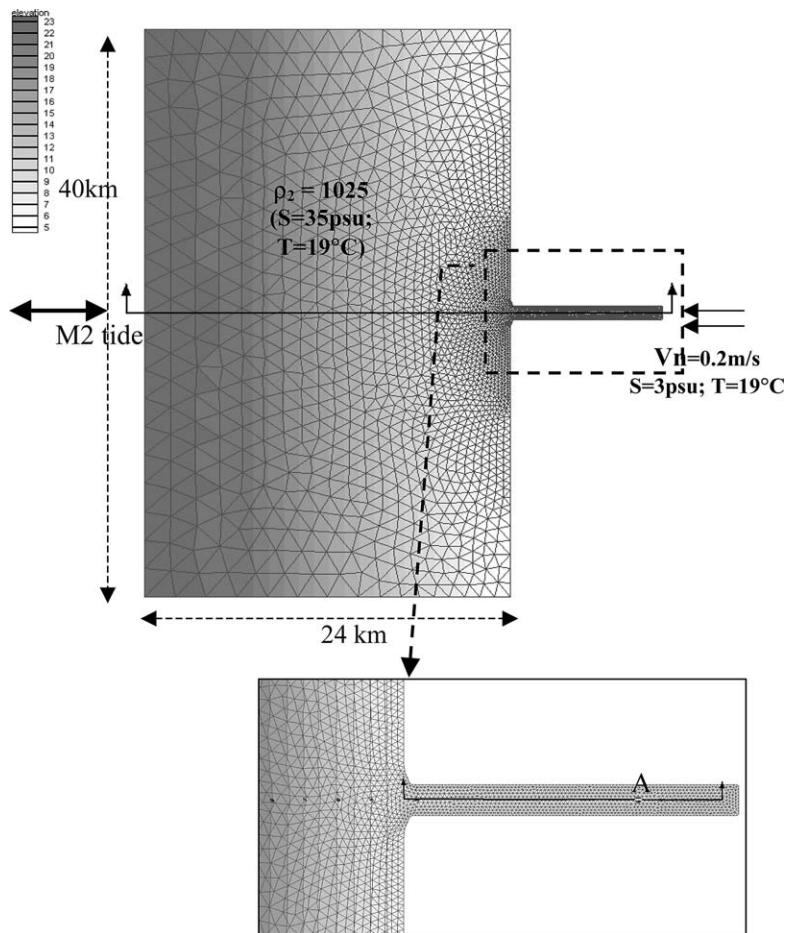


Fig. 2. Configuration of idealized river–ocean domain. Lower figure is a close up part of the dashed-box indicated in the upper figure.

constant velocity 0.2 m/s. The selection of small tidal amplitude is intended to avoid the oscillation of the saline wedge along the river. The initial condition of the domain has uniform salinity $S_0 = 35$ psu and temperature $T = 19^\circ\text{C}$ in the ocean part, while the river flow produces ‘freshwater’ inflow with salinity $S_r = 3$ psu and temperature $T_r = 19^\circ\text{C}$. The salinity gradient between ocean and river generates the pressure gradient due to salinity (i.e. density) difference.

In this case, the prevailing stratification and existence of density gradient will generate a baroclinic flow that drives an upstream flow in the lower layers of the river. This flow contributes to the development of a saline wedge. The balance between outward river flow to the ocean and inward flow into the river due to the baroclinic term provides a nearly steady point at the bottom of the penetrated saline wedge upstream. When the stability of hydrodynamic flow is achieved, the end tip of saline wedge consequently should shift up- and down-stream periodically in coherence with the period of the driving tidal current. Driven with only 0.1 m of M2 tidal amplitude, it is found that the distance range of that periodic shifting is within the range of less than 200 m.

Fig. 3 (a–c) shows vertical profiles of developed saline wedge due to freshwater influx from the river out to the ocean at the end of first, fifth and 10th days,

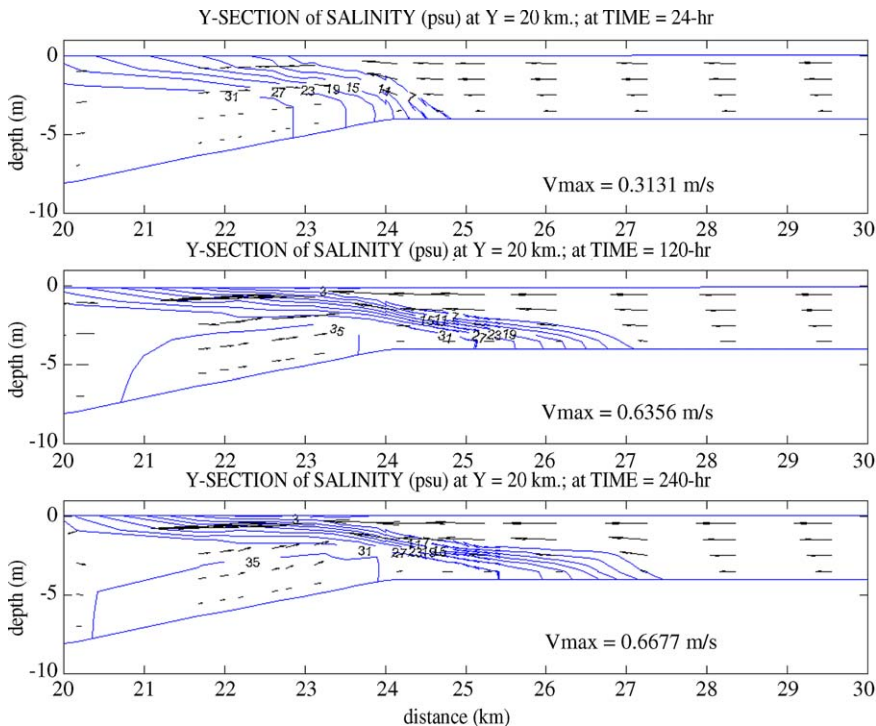


Fig. 3. Side-view profiles of salinity along the transect indicated in the top figure of Fig. 2, during the developed saline wedge at $t = 1$ st day (top), 5th day (middle) and 10th day (bottom).

respectively. The profiles represent a transect along the middle of the river in the x -axis direction indicated in Fig. 2. The upper layers exhibit strong outward flow immediately outside the river mouth and weakened conditions offshore. The maximum outward flow occurs at the river mouth with 0.67 m/s maximum velocity. Meanwhile the inward flow to the river develops the saline wedge with penetrating distance up to about 3.1 km upstream. In the first day, the stratification starts to occur, with less than 1 km of penetration upstream. After 5 and 10 days, the saline wedges are well developed with not much change of the wedge length between the fifth and 10th day.

Empirical computation of saline wedge travel was formulated by Partheniades (1990). He gives various lengths of penetrating saline wedge based on the outward river velocity and river depth (Fig. 4). The formula, which is also known as Schijf and Schoenfeld's equation, is written as

$$L_w = \frac{2h_o}{f} \left(\frac{1}{5Fr_o} - 2 + 3Fr_o^{(2/3)} - \frac{6}{5}Fr_o^{(4/3)} \right) \quad (13)$$

where $Fr_o = V_r / \sqrt{\Delta\rho gh_o / \rho_f}$ is the densimetric Froude number; f is a friction coefficient; h_o is a river depth at river mouth; and ρ_w is the density of freshwater.

The penetration of the saline wedge is estimated graphically from the model results for comparison with the result of Eq. (13). The effective outward flow velocity is averaged from 10 days model observation to remove the effect of tidal oscillation (Fig. 5a). As previously discussed, the specified normal flow is 0.2 m/s; however, due to a slightly widening effect of the river width as it flows into the river domain, the effective averaged velocity decreases to 0.178 m/s. This value is then considered as the outward river velocity to compute the length of theoretical saline wedge (see Table 1). This gives the length of saline wedge 3.11 km.

The corresponding length of saline wedge from the model is estimated from the last simulation day. Fig. 5b shows the near bottom current velocity sampled every

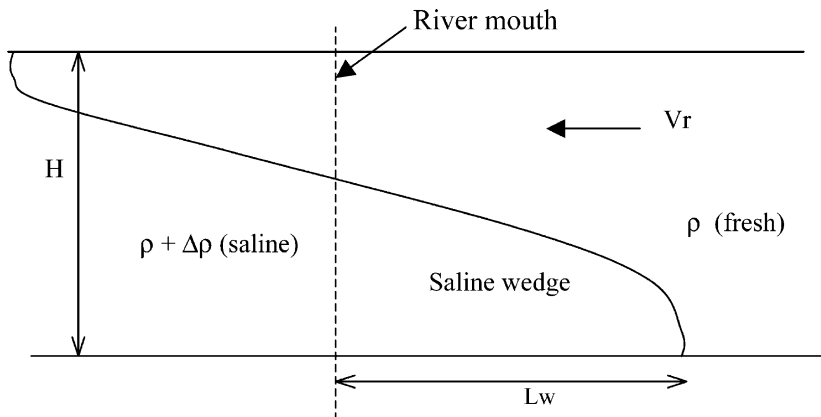


Fig. 4. Saline wedge; L_w is the length of saline wedge computed from the river mouth.

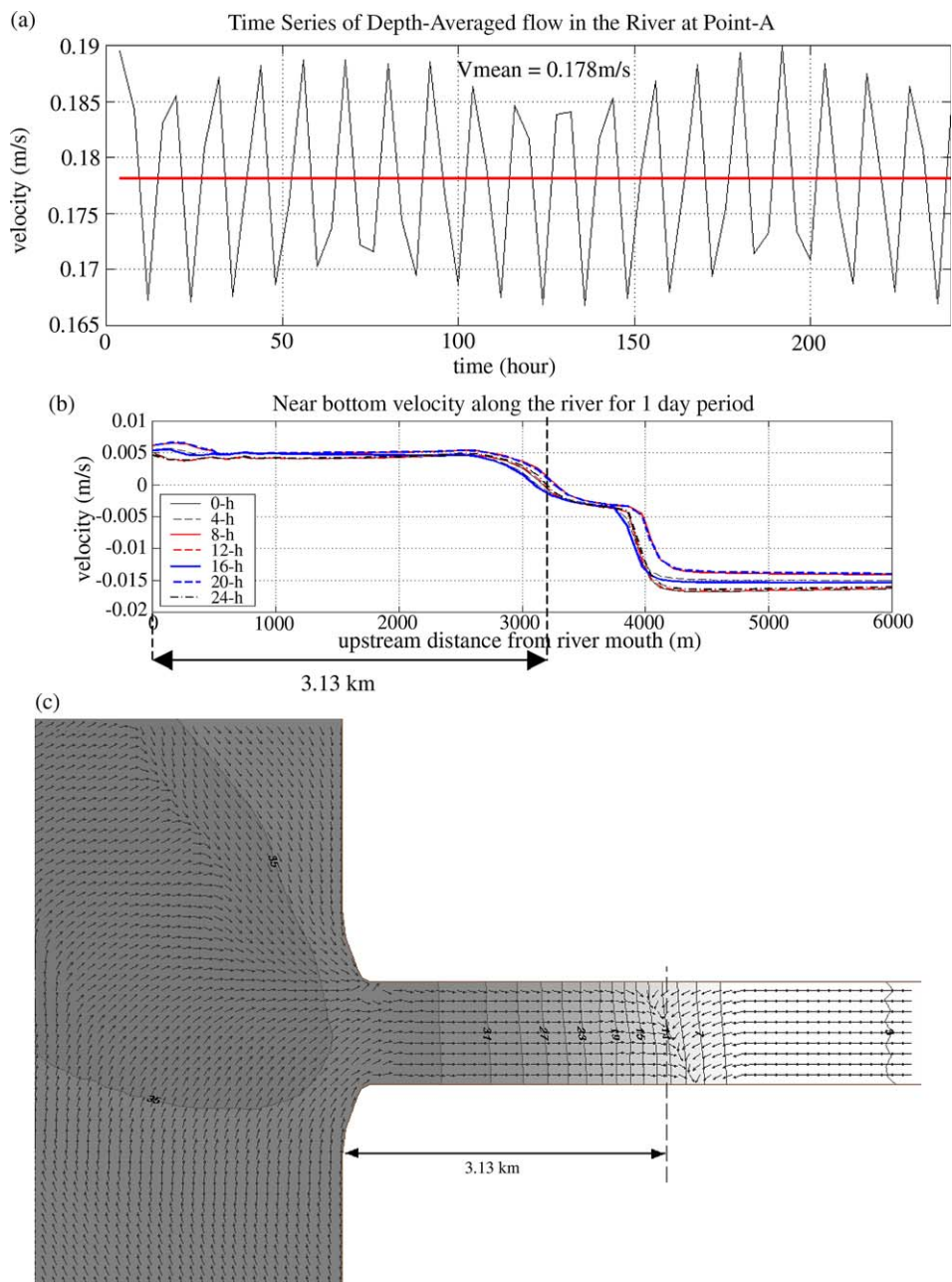


Fig. 5. (a) The assessment of finding the detided depth averaged river out flow from V_r ; (b) Near bottom velocity around the 'null point', where the mean location of zero crossing indicated by the dashed line is 3.13 km from the river mouth; and (c) is the top view of the location of estimated null point. Arrows indicate the flow direction, and contour indicates salinity value.

Table 1
Length of saline wedge for various V_r and h_o

V_r (m/s)	h_o (m)	L_w empirical (km)	L_w numerical (km)
0.10	4.0	10.41	8.14 ^a
0.18	4.0	3.11	3.13
0.18	5.0	5.93	5.84
0.20	2.0	0.44	0.47
0.20	4.0	2.46	n/a
0.20	5.0	4.18	n/a

^a The wedge cannot penetrate further upstream due to the domain limit of 10 km river length.

4 h, from ninth day 0:00 h to 10th day 0:00 h, along the center of the river starting 00 m from the river mouth to the upstream direction. Positive values indicate the upstream flow, while negative values for downstream flow. Fig. 5c gives a top view of the direction of the flow along the river. The zero crossings indicate the location of the ‘null point’, or limit of penetration where the bottom velocity reverses direction, at each particular time. Averaging the location for 24 h provides the estimated length of arrested saline wedge as 3.13 km. For a second case, the river depth is modified to 5 m depth (Table 1, but figure is not shown). The model computes for this case that the length of saline wedge is 5.84 km, while the empirical model gives 5.93 km. Thus comparison between numerical and Partheniades empirical models for the various lengths of saline wedge shows good agreement.

4. Conservation of mass for sediment

To test the capabilities of the model to simulate transport, a simple sloped bottom rectangular domain with a shallow bar located in the middle of the basin was developed as given in Fig. 6. The open ocean boundary is located in the left (west) side of the domain; the normal flow boundary is located in the right (east) side, while the other two sides are defined as mainland (solid) boundaries. The dimensions are 12 km long and 4 km wide, with the 1 m depth of a sand bar located between 8 and 9 km from the ocean boundary. The bay dimension behind the bar ($x = 9$ –12 km) has uniform depth of 2.5 m, while from the bar to the open ocean boundary slopes from 1 to 20 m over 8 km. The triangular grid size was specified to be 125 m along the x -axis and 250 m along the y -axis, giving the number of nodes and elements of 1699 and 3079, respectively. Nine vertical layers are implemented in this simulation which are distributed uniformly in the vertical σ -layers from $\sigma = -1$ at the bottom to $\sigma = 1$ at the surface.

The grid was selected for the analysis of the conservation of mass for the sediment transport. The 3D hydrodynamic model applies one-day ramp function to reach its designed hydrodynamic flows. To assess the conservation of mass for cohesive sediment, the simulation is driven with constant velocity of 1.0 m/s of normal inflow, and zero tide at the open boundary. Starting at the bottom slope of the bar, velocity will increase causing the increase of the bottom stress. Erosion

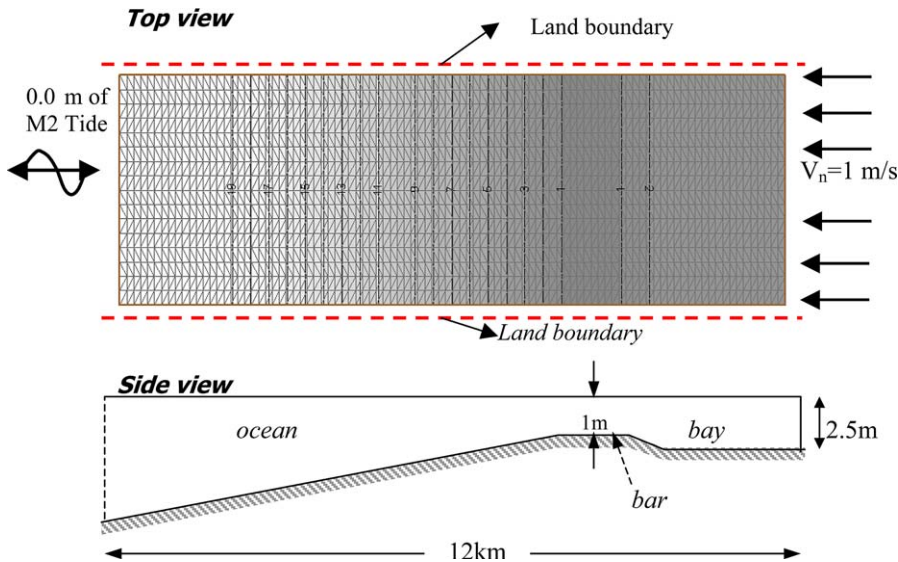


Fig. 6. The configuration of barred rectangular basin. (Upper) The grid consists of 1699 nodes and 3079 elements and the bathymetric depth varies from 1.0 to 19.0 m. Open ocean and normal flow boundaries are specified on the left and right side, respectively. (Lower) The side view of the basin, 12 km long and 4 km wide.

occurs when the bottom shear stress τ_b has exceeded the critical shear stress for erosion τ_{cre} .

Fig. 7 shows the along-basin vertical profile of the sediment transport results at 3D simulation for a cohesive sediment type. The profiles represent the mid-line of the basin (i.e. $y = 2000$ m). The erosion is arbitrarily stopped after 24 h, then it is expected that the amount of depth-integrated suspended sediment plus deposited sediment must be constant. The results are given in Fig. 7 at time $t = 28$ h. Fig. 7b describes the depth-integrated concentration (C_i) of suspended sediment in the water column at each node. The concentration of suspended sediment in units of gram per liter in Fig. 7a is depth-integrated and converted to volume given in units of m^2 (Fig. 7b), which represents the mass volume per width (m^3/m). The corresponding profile of erosion and deposition is given in Fig. 7c. Arrows indicate the direction and magnitude of 3D flow components.

Assuming the distribution of transport is uniform across the basin, the simple way to estimate the conservation of mass is to compute the area along the profile with the expected relationship:

$$\text{Erosion (m}^2\text{)} = \text{Depth-integrated suspended sediment (m}^2\text{)} \\ + \text{Deposition (m}^2\text{)}$$

Thus, from Fig. 7 middle and bottom, one would expect that $C_i + \text{Depo} = \text{Ero}$, but the results are not acceptable. The finite element method for solving the gov-

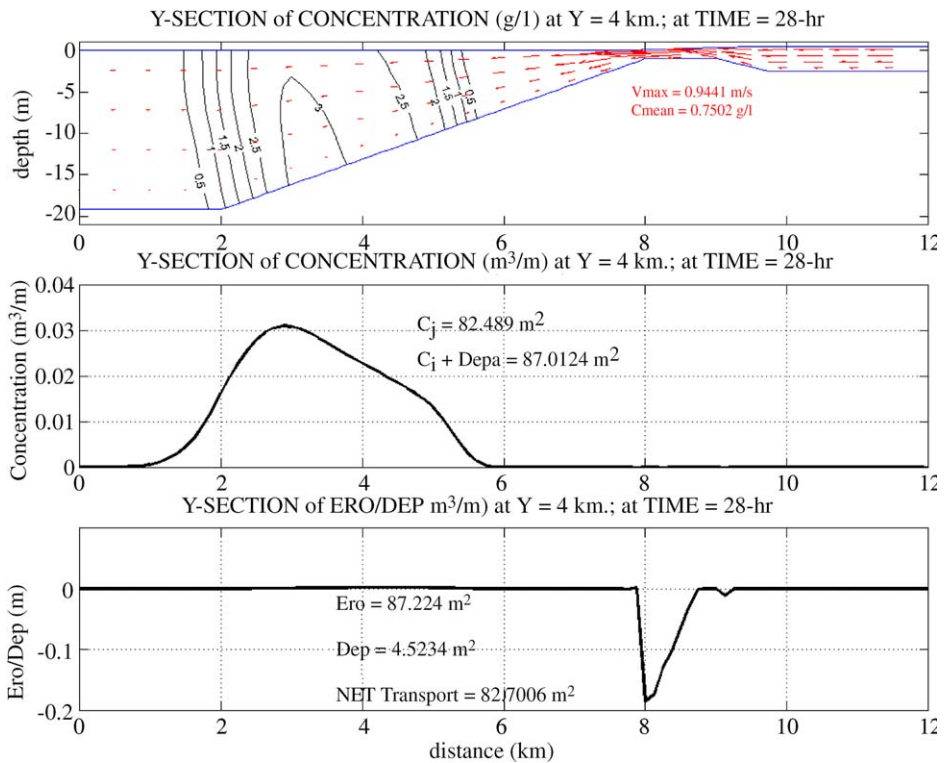


Fig. 7. Profile of cohesive sediment transport taken at time $t = 28$ h. (a) Contour plot of suspended sediment concentration with arrows representing the relative magnitude and direction of current velocity; (b) Depth-integrated concentration along the profile in term of m^2/m ; and (c) the corresponding erosion (–) and deposition (+) along the profile line.

erning equations is usually conserved locally, but not globally. Small numerical rounding errors might propagate from element to element and develop accountable errors. Conversion of vertical reference from z - to σ -level can introduce another source of conservation errors as it was discussed in Mellor et al. (1998).

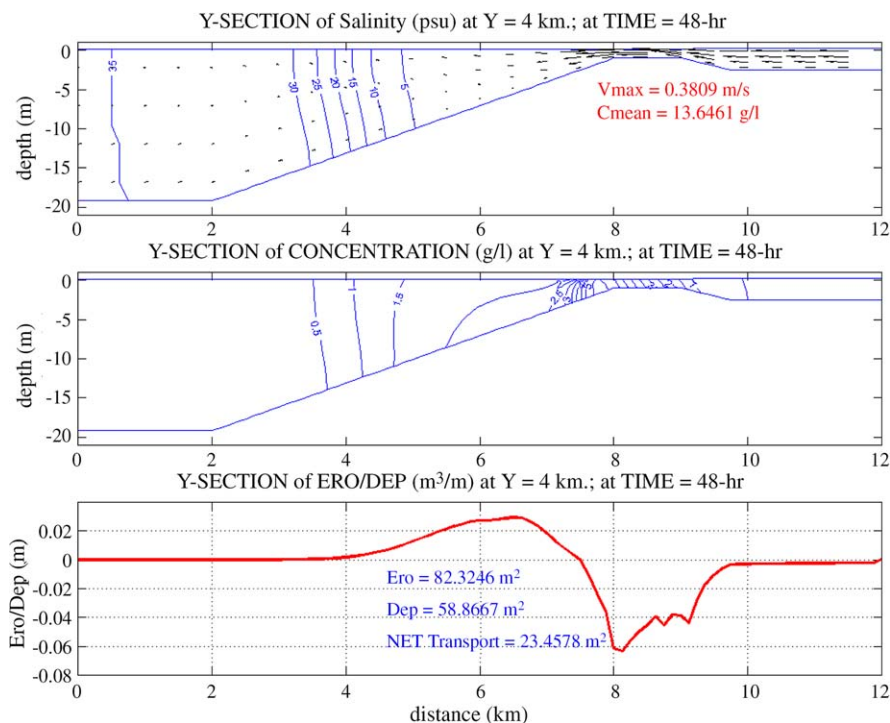
It is commonly known that cohesive sediment in a bed is very easily eroded and suspended when τ_b exceeds τ_{cre} , transported in a relatively long distance, and deposited back to a bed at particular location whenever the τ_b is less than τ_{crd} . The amount of suspended sediment is high and settles slowly due to slow settling velocity computed using Eq. 9. The existing very shallow bar of 1 m produces a maximum horizontal velocity of about 0.95 m/s near the left tip of the bar where the maximum erosion occurs. In Fig. 7a, after the erosion is arbitrarily forced to stop at $t = 24$ h, the cloud of cohesive suspended sediment travels offshore while the particles tend to settle down. Thus the prevailing sediment concentration should be high at near bottom decreasing upward to the surface. The error in this simulation is less than 1% of the transported mass volume. The error of

conservation of mass for cohesive sediment is usually less than 2%, especially in the sloping bottom. The sources of the error are commonly due to accumulative numerical accuracy either from hydrodynamic or transport modules.

5. Barotropic versus baroclinic modes

Coupling the baroclinic hydrodynamic circulation and sediment transport in the stratified water is the main goal of this study. A comparison between barotropic and baroclinic modes of sediment transport is performed to assess the importance of the baroclinic term.

Fig. 8a describes a snapshot taken at $t = 48$ h of the salinity contour of barotropic transport mode for cohesive type sediment. The setup configuration of the model is similar to the previous cases with the barred rectangular basin, but the open boundary is driven with larger 0.5 m M2 tidal amplitude, and allowing the erosion to occur continuously. The freshwater discharge from the normal flow boundary on the right propagates towards offshore in nearly vertically uniform



transport, indicated by the uniform density (i.e. salinity) distribution. Consequently, the eroded cohesive sediment along the top of the bar is also suspended and transported nearly uniformly, but there is a relatively small settling velocity taking place during the transport causing higher concentration near bottom immediately after it is suspended (Fig. 8b). The vertical profile of horizontal velocity has higher velocity in the mid to top column than at bottom. Thus, the upper layers will travel faster than the bottom layers. Combining with the diffusion and vertical advection taking place during the horizontal transport, the sediment distribution is likely to become more uniform at the location far away from its origin. Here, the critical stresses for erosion (τ_{ce}) and deposition (τ_{cd}) are 0.2 and 0.1 N/m², respectively.

As in previous case, the model applies one-day ramp function to reach its designed hydrodynamic flows. The initial erosion occurred before the full ramp function is achieved, and the site of deposition is at some distance offshore from the erosion site due to the difference in the τ_{ce} and τ_{cd} . After the hydrodynamic ramp function, the erosion site is shifted further offshore than previously. Since the erosion and deposition processes occur almost continuously, as shown in Fig. 8c, there is likely continuous erosion followed by immediate deposition onshore.

Another simulation was performed similar to the formerly discussed case with similar setup and configuration, but with activating both the baroclinic and barotropic terms, later the so-called baroclinic mode (Fig. 9). It creates a significantly different mechanism of sediment transport for the cohesive type sediment. Due to freshwater ($S = 3$ psu) discharge from the normal flow boundary on the right side of domain into the saline ocean water ($S = 35$ psu), the presence of stratification is clearly seen when the baroclinic term is activated (Fig. 9a).

The tip end of saline wedge is located in the x -axis between 6 and 6.5 km. At the end tip of saline wedge, the near bottom horizontal velocity is small, but upward vertical velocity increases causing the near bottom sediment to either settle down or be lifted up. In the case of cohesive sediments, the concentration of suspended sediment is small, thus the settling velocity is relatively smaller than its vertical lift velocity. Once the sediment is suspended and lifted up, the path of transport will be mainly driven by baroclinically hydrodynamic flow causing a cloud of suspended sediment concentrated in the top layers (Fig. 9b). The suspended sediment cloud will be either carried away outside the domain or deposited at some points further away offshore.

The processes of erosion and deposition around the top of the bar are almost similar between baroclinic and barotropic modes; however, at points at $x = 5.8 - 6.2$ km in Figs. 8c and 9c, it is clearly seen that less deposition occurs in the baroclinic mode around the tip of saline wedge, some amount of suspended sediment is raised up becoming a cloud of upper layer suspended sediment. The amount of erosion, deposition and net sediment transport between those two modes are summarized in Table 2.

Thus, in this case, the inclusion of the baroclinic mode allows 60% of eroded materials to remain in suspension after 48 h, while the barotropic mode transports only about 28% of eroded materials in the water column after 48 h.

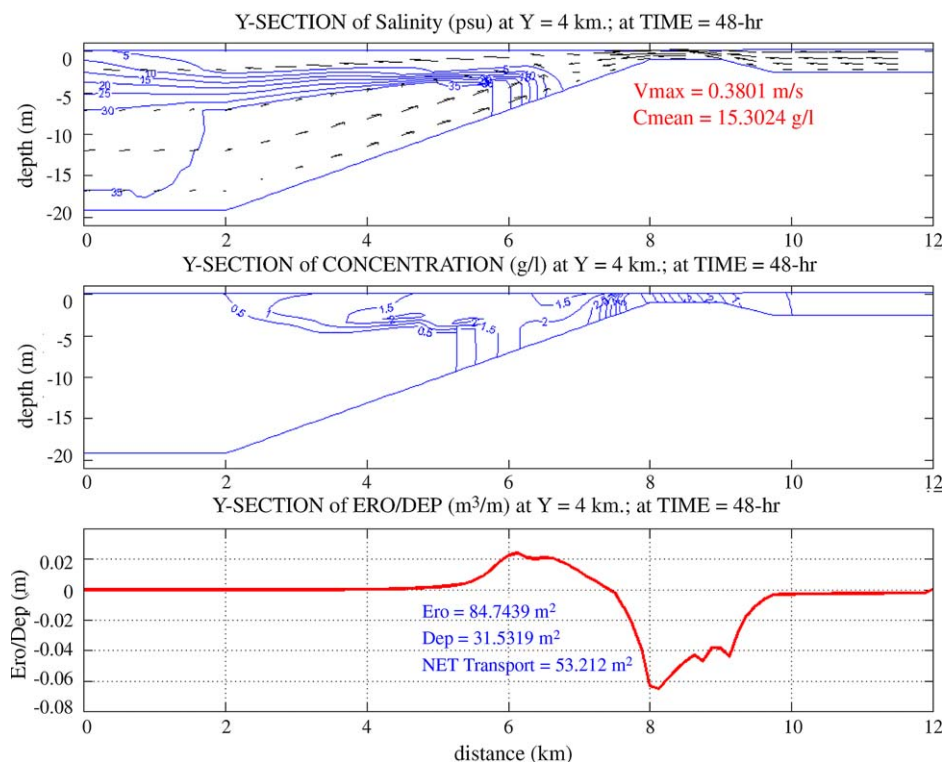


Fig. 9. Profile of cohesive sediment transport, *baroclinic* mode, taken at time $t = 48$ h. (a) Contour plot of salinity in psu units with arrows representing the relative magnitude and direction of current velocity; (b) Contour plot of suspended sediment concentration; and (c) the corresponding erosion (–) and deposition (+) along the profile line.

Table 2

Comparison of sediment transport between barotropic and baroclinic modes of sediment transport at $t = 48$ h

	Erosion (m ³ /m)	Deposition (m ³ /m) (% of erosion)	Net transport (m ³ /m) (% of erosion)
Baroclinic mode	84.744	31.532 (37%)	53.212 (63%)
Barotropic mode	82.325	58.867 (72%)	23.456 (28%)

6. Idealized tidal inlet

An additional case was made to simulate the behavior of sediment transport with baroclinic mode in an idealized tidal inlet with the domain shown in Fig. 10. The ocean grid dimension is 24 km alongshore, and 24 km from the shoreline to the ocean boundary. The inlet length and width are 1.5 and 1.125 km, respectively;

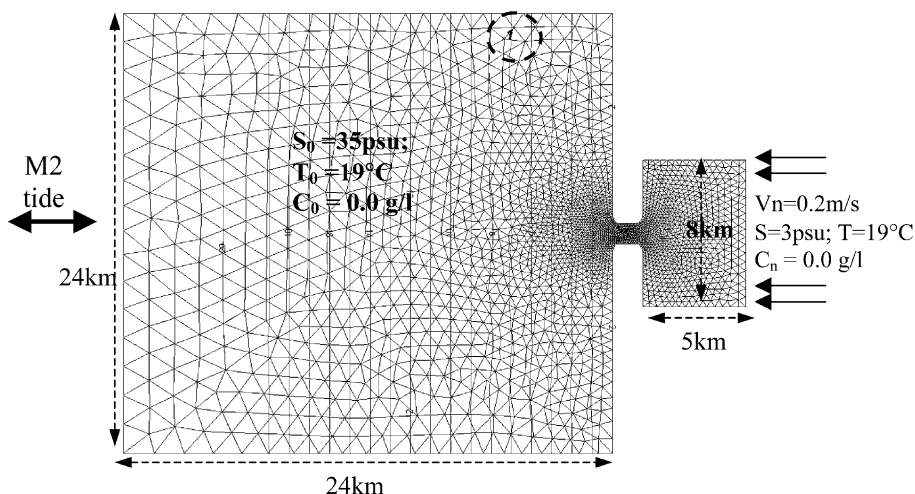


Fig. 10. Bathymetry and triangular grid of an idealized tidal inlet. Point-1 (dash-circled) is the selected point to assess the longshore sediment flux.

and bay dimensions are 5×8 km, with uniform depth of 2 m. The ocean depth was specified 2 m along the shoreline down to 20 m along the open boundary. The triangular grid sizes were specified to be 75 m around the inlet, gradually increasing toward the open boundary to the size of 1500 m. The final grid contains 2397 nodes with 4575 triangular elements.

The model is driven with semidiurnal M2 tide with 0.4 m tidal amplitude at the open ocean boundary. The north and south border of the domain are defined as the normal radial wave boundaries with no constraints applied along those two boundaries. The coastlines to the north and to the south of the inlet, around the inlet and the north and south of the bay are defined as the mainland boundaries. Essential normal flow boundary conditions are applied along the east side of the bay, with constant normal velocity $V_n = 0.1$ m/s. The vertical is divided into 9 σ -layers that are uniformly distributed from bottom to surface as $\sigma = [-1, -0.75, -0.5, -0.25, 0.0, 0.25, 0.5, 0.75, 1.0]$.

The initial conditions of salinity, temperature and sediment concentration in the ocean side are set to $S_o = 35$ psu, $T_o = 19^\circ\text{C}$ and $C_o = 0.0$ g/l, respectively; while in the bay the initial condition for those parameters are $S_o = 3$ psu, $T_o = 19^\circ\text{C}$ and $C_o = 0.0$ g/l. Along the normal flow boundary, the normal flux of salinity, temperature and concentration are set as the essential scalar flux with $S_n = 3$ psu, $T_n = 19^\circ\text{C}$ and $C_n = 0.0$ g/l. The model performed a 10-day simulation with hydrodynamic time step $\Delta T = 4$ s and transport time step $\Delta T_{tr} = 12$ s. One day hydrodynamic and three-day baroclinic ramp functions are applied to initiate the simulation. The implementation of the baroclinic ramp function is intended to smooth the initially sharp salinity gradient between fresh and saline waters. Thus, in this case the fully baroclinic term is achieved after three-day simulation. The

salinity gradient between the surface and bottom layers will generate a density pressure gradient, and balanced by the Coriolis force will develop a geostrophic current northward if one assumes the northern hemisphere.

After 10-day simulation, the salinity front is well developed. Fig. 11 shows a comparison of salinity distribution between near surface ($\sigma = 0.75$) and near bottom ($\sigma = -0.75$) layers. Near surface salinity spreads much further offshore developing a tongue of low salinity propagating northward, with its center of low salinity about 8 km offshore. The distribution of salinity further offshore is accelerated by two factors: (1) momentum flux from the normal flow on the right boundary, and (2) offshore acceleration of the baroclinic term in the upper layers due to the presence of the salinity (i.e. density) gradient.

The near bottom layer salinity clearly exhibits different pattern of salinity distribution. Due to the balance between upstream baroclinic forcing in the lower layers, the salinity front in near bottom layer does not propagate far offshore, but just in the outer tip of the inlet. The front oscillates back and forth along the inlet in accordance with the tidal period. However, there is a northward propagation of brackish water with salinity value from 19 to 33 psu that is caused by the presence of northward-developed geostrophic transport along the shore. It is imminent that the distribution of near bottom salinity becomes asymmetry from the inlet to the offshore.

In the near surface layer, about 2 km offshore of the inlet, there is a small circular area having salinity higher than its surrounding area. This area represents the convergence/divergence zone between freshwater fluxes and tidally oscillated saline water where vertical mixing is intensively occurring in this area in coherence with tidal oscillation. The high salinity in the indicated area is caused by the supply of the saline water from the lower layer by an upwelling process. However, further assessment is necessary whether this area does observable in any real bodies of water.

The corresponding sediment transport nearly follows the pattern of the salinity transport, except that the sediment experiences settlement as it is transported, and it is deposited when the bottom shear stress is less than its critical shear for deposition, τ_{crd} (see Fig. 12). The channeling effect of the normal inflow from the east-end boundary into the bay and then through the inlet will significantly increase the current velocity along the inlet. Consequently, the bottom shear stress increases and the source of suspended sediment is initiated by the erosion occurring in the inlet. The suspended sediment is then transported offshore and deflected northward due to the effect of developed geostrophic transport discussed previously. The maximum suspended concentration in the near surface layer is 0.5 g/l in the inlet and decreases to 0.025 g/l at about 8 km offshore. Similar to the salinity, the distribution of the near surface sediments also experience right-deflected propagation due to the prevailing Coriolis force acting on the water mass.

The maximum concentration near the bottom layer is higher than the layers above since settlement of suspended sediment drives the concentration to accumulate in the bottom layers. Sediments from the inlet are transported downstream, and because of settlement they reach lower layer and are transported back to the

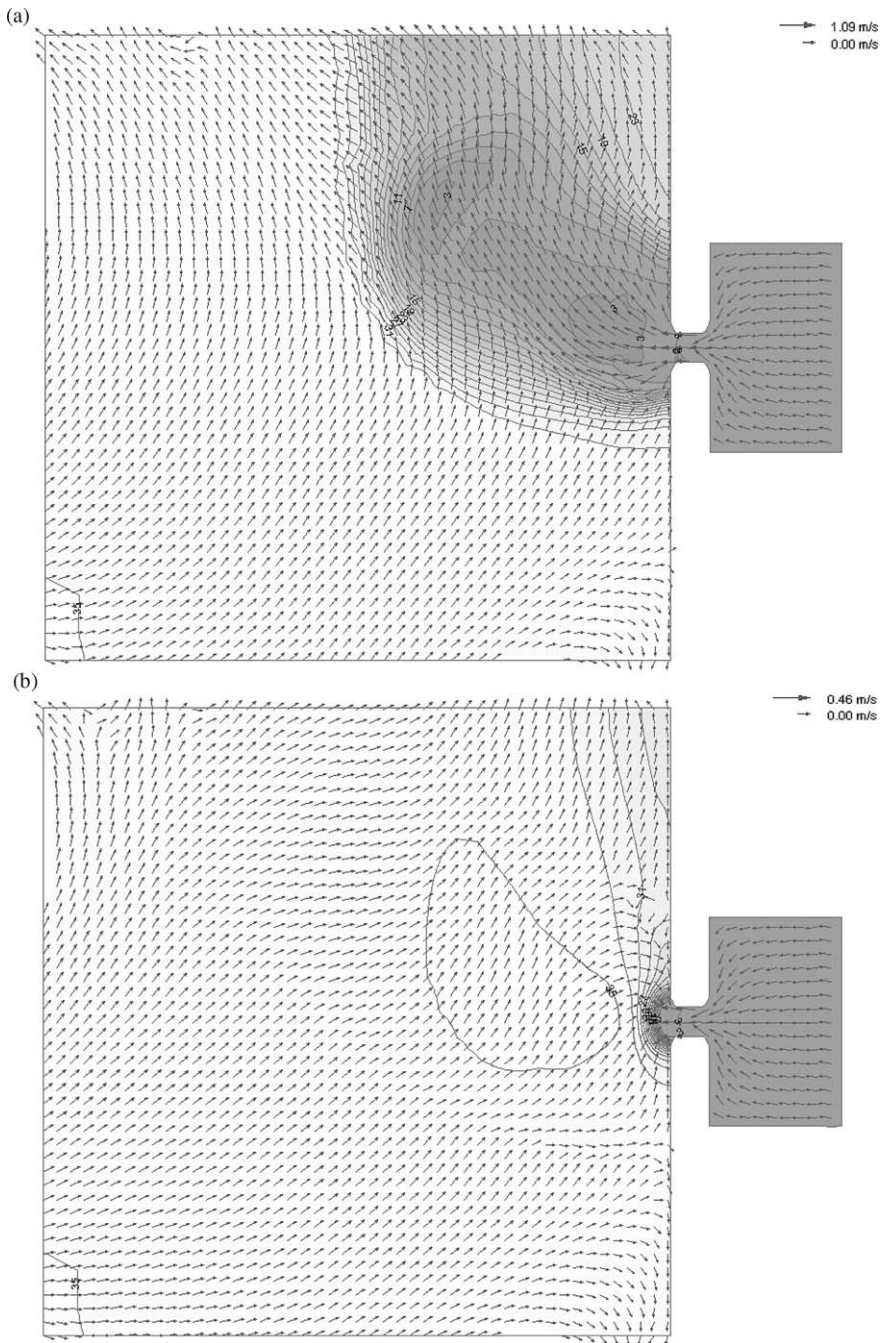


Fig. 11. (a) Near surface salinity; and (b) near bottom salinity; both are taken at $t = 10$ d simulation. Contour lines indicate salinity values, and the scaled arrows represent the direction and magnitude of the flow.

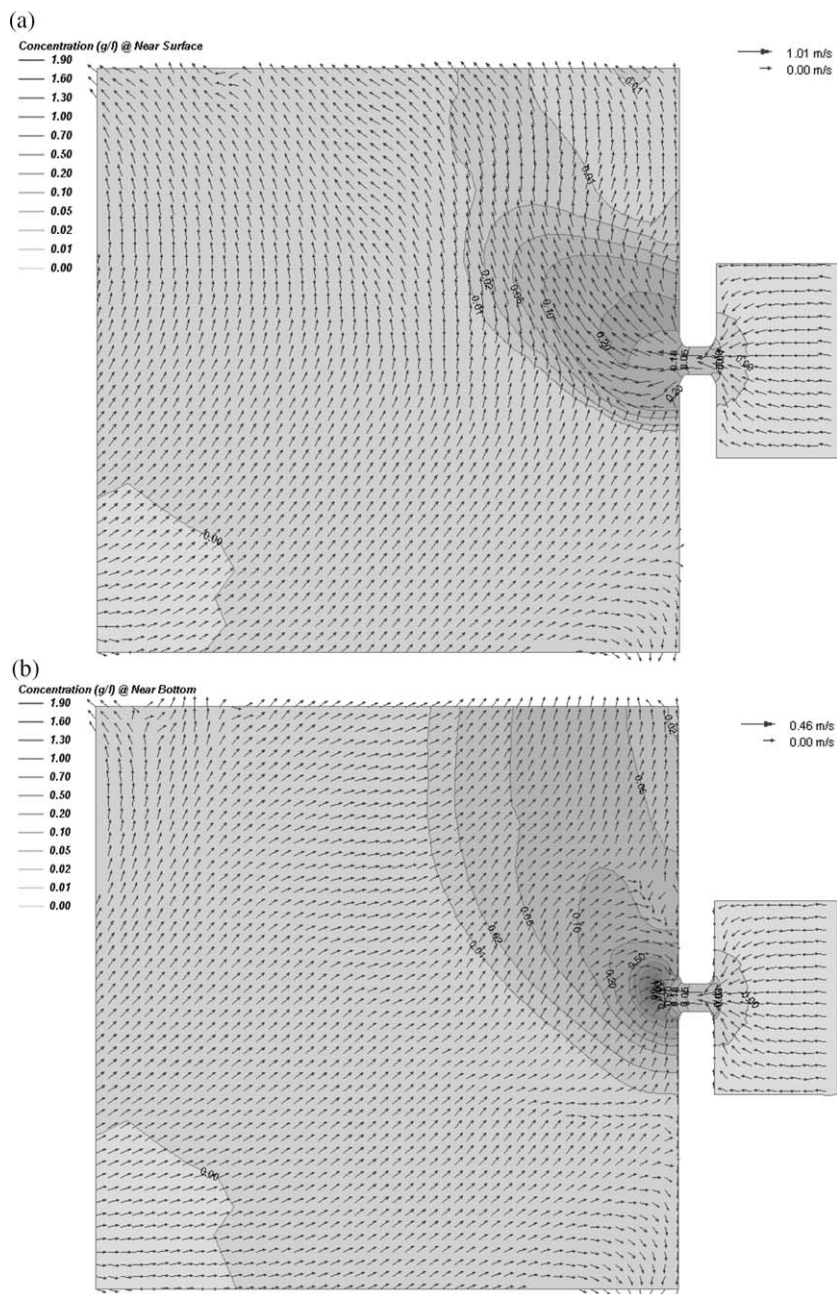


Fig. 12. (a) Near surface concentration of suspended sediment; and (b) near bottom concentration of suspended cohesive sediment; both are taken at $t = 10$ d simulation. Contour lines indicate concentration in g/l, and the scaled arrows represent the direction and magnitude of the flow.

upstream by the residual flow in the lower layer to the convergence point, the so-called ‘null point’. The highest near bottom sediment concentration is 1.94 g/l concentrated near the mouth of the inlet in the offshore direction. This site is related to the place where null point occurs. However, the prevailing northward longshore currents transports some residual sediments to the north.

Interpolation from irregular (Fig. 10) to regularly rectangular grid was performed to generate a matrix for 3D view. The result for the suspended sediment concentration is shown in Fig. 13 taken at $t = 10$ day. It is clearly shown that the high concentrations are mostly suspended around the mouth inlet seaward not far away from the origin of erosion. As the sediment cloud deflected to propagate northward, the concentration becomes less and less. Higher concentration is contained in the lower layer.

It is expected that for longer simulation times, the longshore transport would move this cloud of sediments much further northward; but this is beyond the scope of discussion in this paper. For cohesive sediment, decreasing suspended sediment concentration will reduce the settling velocity (Eq. (9)), thus the sediment will likely remain suspended in the water column much longer. To investigate the prevailing

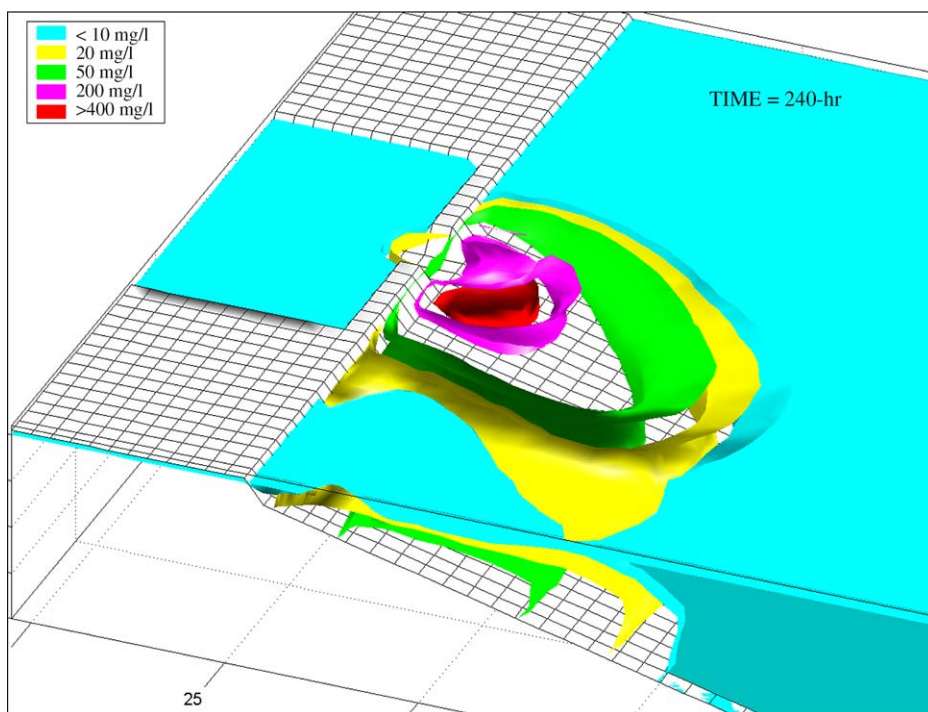


Fig. 13. Three-dimensional view of suspended sediment concentration (in mg/l) observed from azimuth -20°N . The plot is taken at $t = 10$ -day simulation. Rectangular grids represent the surface of the bathymetry.

northward flow, one point, marked as ‘Point 1’ (dash-circled in Fig. 10) is selected at near north radial boundary. The depth averaged of east–west (U) and north–south (V) flow directions are shown in Fig. 14a and b, respectively. Detided time series provides nearly zero eastward flow and 0.07 m/s northward flow after 10-day simulation. The nearly zero flow in the eastward flow may indicate that there is only a small cross-shore transport as the material was injected through the inlet; on the other hand, the presence of net northward flow may lead a significant long-shore transport of suspended sediment. The depth averaged northward flow increases as the salinity difference between near shore and offshore location becomes more prominent. Such a difference causes the baroclinic acceleration to be enhanced.

The corresponding time series of the depth-integrated concentration in units of kg/m^2 is given in Fig. 14c, where the concentration at point 1 tends to increase as the supply of suspended sediments from the inlet are transported alongshore from the south. The concentration here is the residual sediment transport that has not yet deposited and remains as a suspended sediment. The net of depth-integrated

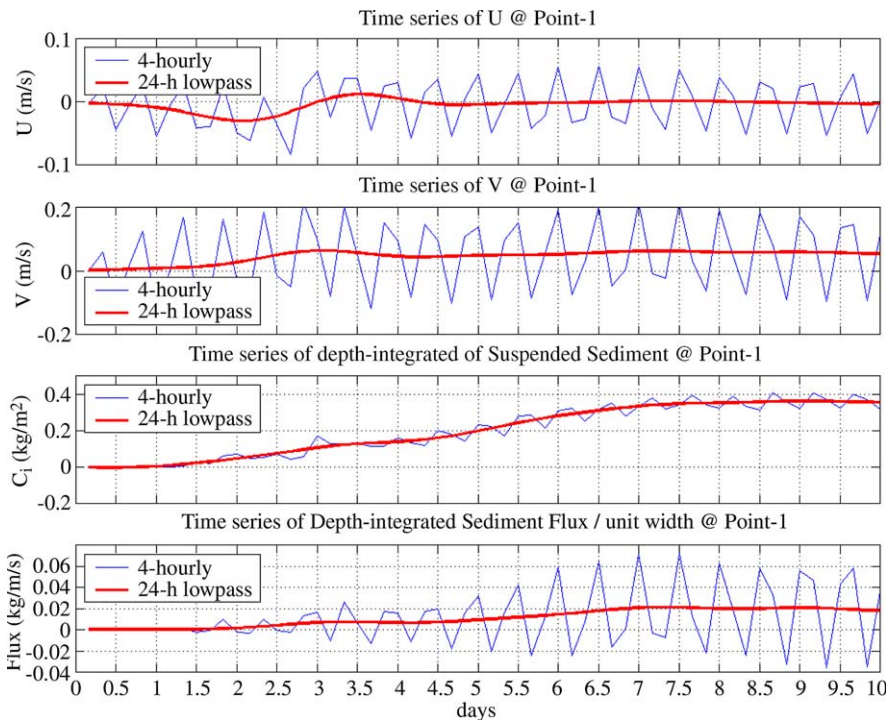


Fig. 14. (Top–bottom) Time series of depth-averaged velocity U and V , depth-integrated suspended concentration, C_i , and depth-integrated sediment flux at point 1 indicated in Fig. 10. The thin lines represent the observational values obtained from the model, and bold lines are detided values (24-h low passed) of each constituent.

sediment flux shown in Fig. 14d is computed by multiplying the depth-integrated concentration with its prevailing northward flow. The unit of the sediment flux is $\text{kg/s/m}_{\text{width}}$. In this study case, it is demonstrated that due to existing erosion around the inlet may provide a net longshore sediment transport of 0.018 kg/m/s .

The maximum seaward velocity passing the inlet occurs near the ocean side end of both left and right edges of the inlet (Fig. 15). The maximum erosion at those sites is more than 0.08 m for the period of 10 days. The erosion is fairly uniform in the middle of the inlet of about 0.06 m decreasing towards east and west sides of the inlet.

The deposition pattern is asymmetrical between the ocean and bay sides, with more significant deposition occurring at the ocean side. The main deposition of suspended sediment is mainly concentrated just offshore of the inlet mouth indicated by a dark shade in Fig. 15, with its maximum deposition of about 0.04 m accumulated for a 10-day simulation, or about 1.4 m/year . This area represents the null-point zone between the out flow jets from the inlet and inward saline wedge due to the presence of the baroclinic flow. The saline wedge does not penetrate the inlet due to strong inlet out flow. Thus, the existing null point may trap the near bottom sediment to settle and deposit at the bottom, meanwhile the upper layer

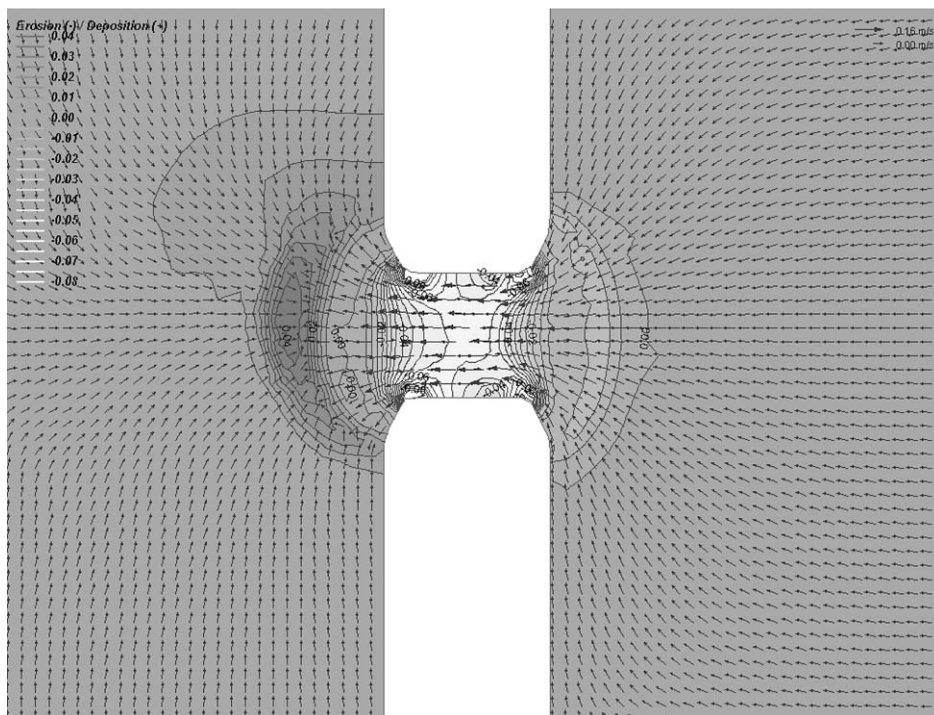


Fig. 15. The erosion (–) and deposition (+) after 10-day around the inlet.

concentration tends to be transported further, deflected to the right, and carried away by the prevailing longshore geostrophic flow previously discussed.

7. Summary and conclusion

A numerical model for simulation of hydrodynamic circulation and sediment transport is described in this study. The model includes baroclinic forces to incorporate density changes found near the coast. The model has been applied to several test cases to demonstrate its applicability to practical problems and to demonstrate its robustness.

Comparison of the arrested saline wedge from the numerical model to the empirical formulation gives a good agreement. The computational saline wedge using the Partheniades empirical formulation is very sensitive to the change of both river flow and depth. Thus, very accurate assessment of the model results is required to demonstrate that penetration of saline wedge agrees with empirical data. The method of finding the length of arrested saline wedge is efficiently demonstrated here by finding the null point at near bottom velocity profile.

The inclusion of the baroclinic term in the model for the stratified estuary contributes to wider distribution pattern of suspended sediment, mainly for cohesive type sediments. To reach the stability condition for large horizontal salinity gradient (i.e. large density gradient) between fresh and saline water, the baroclinic ramp function is required to smooth the baroclinic acceleration term. A high horizontal diffusion coefficient, D_h , up to $20 \text{ m}^2/\text{s}$ might also be required; however, in most cases of stratified waters the D_h value less than $10 \text{ m}^2/\text{s}$ should be sufficient.

The conservation of mass is well established in the model with accuracy up to 2% error of the conserved mass. The simulations show that a flat bottom provides better conservation of mass than a sloping bottom. The effect of slope may lend a source of the error, and it needs to be investigated further. However, the model is mostly applicable for estuarine zone with fairly gentle slopes. Therefore, the error discussed is considered to be acceptable to model the sediment transport in the near shore or estuarine zone.

The transport model is able to describe a realistic cohesive sediment transport with the influence of the baroclinic term. The study case for an idealized tidal inlet exhibits reasonable mechanism of erosion, suspended sediment and deposition. As expected, the location of the deposition occurs mostly around the null-point location. The pattern of deposition clearly shows development of an ebb shoal. Longer run-time simulation might be required to investigate the ebb shoal development around the offshore side of the tidal inlet.

Salinity difference between ocean water and freshwater discharge from the inlet clearly generates very strong density gradients that also generate the geostrophic flows. After removing the tidal effect, the model has been able to demonstrate the presence of the longshore sediment transport associated with the existing geostrophic flow. This may lead to future application to study of the freshwater and suspended sediment discharges of Mississippi River to the Gulf of Mexico where a

significant amount of suspended sediments are transported alongshore towards the Texas coast. Future development includes a benchmarking of the model against the laboratory and observational results.

Acknowledgements

The study described in this paper has been supported in part by the US Environmental Protection Agency through the South and Southwest Hazardous Substance Research Center, the National Science Foundation, and the Texas Engineering Experiment Station at Texas A&M University.

References

- Blumberg, A.F., Mellor, G.L., 1987. A description of a three-dimensional coastal ocean circulation model. In: Heaps, N.S. (Ed.), *Three-Dimensional Coastal Ocean Models*. American Geophysical Union, Washington, DC, pp. 1–16.
- Gross, E.S., Koseff, J.R., Monismith, S.G., 1999. Three-dimensional salinity simulations of South San Francisco Bay. *J. Hydraul. Eng.* 125 (11), 1199–1209.
- Hayes, S.P., Chang, P., McPhaden, M.J., 1991. Variability of sea surface temperature in eastern equatorial Pacific during 1986–88. *J. Geophys. Res.* 96 (C6), 10533–10566.
- Helfand, J.S., Podber, D.P., McCormick, M.J., 1999. Effect of heat flux on thermocline formation. In: Spaulding, M., Butler, R. (Eds.), *Estuarine and Coastal Modeling*. In: *Proceedings of the Sixth International Conference on Estuarine and Coastal Modeling*. ASCE, New Orleans, LA.
- HydroQual Inc., 1998. Development and application of a modeling framework to evaluate hurricane impacts on surficial mercury concentrations in Lavaca Bay. Project Report, Aluminium Company of America, Point Comfort, TX.
- Ippen, A.T., 1966. *Estuary and Coastline Hydrodynamics*. McGraw-Hill, NY.
- Luettich Jr., R.A., Muccino, J., 2001. Summary of vertical velocity calculation methods as considered for 3D ADCIRC hydrodynamic model. Paper on ADCIRC Workshop 20–21 Feb 2001, NRL, Stennis, MS.
- Luettich, R.L., Westerink, J.J., 2003. Formulation and numerical implementation of the 2D/3D ADCIRC finite element model version 43.XX. Paper on ADCIRC Workshop 27–28 Feb 2003, NRL, Stennis, MS.
- Luettich Jr., R.A., Westerink, J.J., Scheffner, N.W., 1992. ADCIRC: An advanced three-dimensional circulation model for shelves, coasts, and estuaries. Report 1. Technical Report DRP-92-6, Dredging Research Program, USACE, Washington, DC.
- Lynch, D.R., Officer, C.B., 1985. Analytic test case for three-dimensional hydrodynamic models. *Int. J. Num. Meth. Fluids* 5, 529–543.
- Mellor, G.L., Yamada, T., 1982. Development of a turbulence closure model for geophysical fluid problems. *Rev. Geophys. Space Phys.* 20, 851–875.
- Mellor, G.L., Oey, L.Y., Ezer, T., 1998. Sigma coordinate pressure gradient and the sea mount problem. *J. Atmos. Ocean. Technol.* 15 (5), 1122–1131.
- Muccino, J.C., Gray, W.G., Foreman, G.G., 1997. Calculation of vertical velocity in three dimensional, shallow water equation, finite elements model. *Int. J. Num. Meth. Fluids* 25, 779–802.
- Pandoe, W.W., Edge, B.L., 2003. Three-dimensional hydrodynamic model, study cases for quarter annular and idealized ship channel problems. *J. Ocean Eng.* 30, 1117–1135.
- Partheniades, E., 1990. Estuarine sediment dynamics and shoaling processes. In: Herbich, J.B. (Ed.), *Handbook of Coastal and Ocean Engineering*, vol. 3. Gulf Publishing Co, pp. 881–984.
- Robertson, R., Padman, L., Levine, M.D., 2001. A correction of the baroclinic pressure gradient term in the Princeton ocean model. *J. Atmos. Ocean. Technol.* 18 (6), 1068–1075.

- Scheffner, N., 1999. A large domain convection diffusion based finite element transport model. In: Spaulding, M.L., Butler, H.L. (Eds.), *Estuary and Coastal Modeling*. In: *Proceedings of the Sixth International Conference on Estuarine and Coastal Modeling*. ASCE, pp. 194–208.
- Whitehouse, R., Soulsby, R.R., Roberts, W., Mitchener, H., 2000. *Dynamics of Estuarine Muds*. H. R. Wallingford, UK.